2025 IEEE/SICE International Symposium on System Integration (SII)
January 21-24, 2025, Munich, Germany

Enhanced Calibration of a Laser Profiler Sensor for 3D Inspection and Reconstruction

Houssein OLLEIK[1,2], Vincent VAUCHEY[2], Ahmed NAIT CHABANE[2], Yohan DUPUIS[2]

***Abstract*— In recent decades, inspection and three-dimensional reconstruction of gas and water pipes have required high-precision sensors capable of operating in confined and low-texture environments, which presents challenges to traditional sensing technologies. This paper presents the design of both hardware and software for a laser profiler sensor, introducing a novel approach to calibrating the sensor to enhance its accuracy and functionality in industrial inspections. We introduce a new calibration method suitable for both conic and planar lasers, with calibration achieved through a two-step process: initial multiposition binocular-structured light calibration and subsequent refinement using a standard ring gauge. The calibration method is uniquely designed to be compatible with both cone- and plane-type calibrations, providing a robust and versatile solution for industrial laser profiling. We demonstrate the efficacy and accuracy of our proposed calibration method, with errors consistently remaining below 1 mm, thus validating the reliability of the reconstruction process.**

I. INTRODUCTION

Recently years, the demand for high-precision inspection and three-dimensional (3D) reconstruction of gas and water pipelines has increased significantly, driven by the need for improved maintenance and safety standards [1]. These tasks require sensors that can operate accurately in confined spaces with low texture, which presents challenges to traditional sensing technologies. One of the most effective sensors for achieving high-precision 3D reconstruction in such environments is the laser profiler [2], [3].

Laser profilers emit a laser line onto a surface and use a camera to capture the reflection, allowing for the 3D reconstruction of the surface with millimeter precision. As shown in Figure 1, the laser source of our sensor, represented by the blue block, directs the laser beam onto a conic mirror inside a 25 cm calibration tube, generating a laser plane. This approach is particularly useful in industrial environments, where accurate inspection of pipes and infrastructure is critical for detecting defects like cracks and corrosion [4].

Despite their effectiveness, laser profilers require precise calibration to ensure the accuracy of the 3D models they generate. Calibration involves determining the exact relationship between the laser line and the camera's field of view.

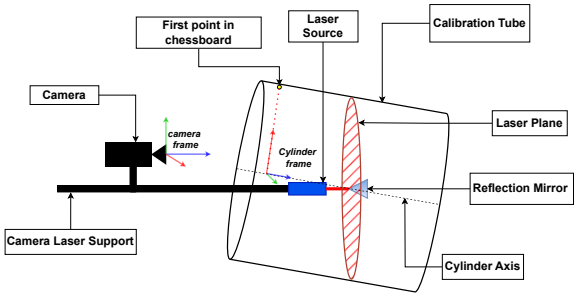

Fig. 1: Calibration Procedure For The Laser Profiler.

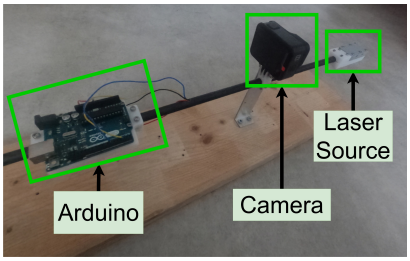

Fig. 2: Our Laser Profiler Sensor.

This study proposes a new method for designing and calibrating a laser profiler sensor that seeks to improve its precision and effectiveness in industrial inspections. We present an advanced calibration technique that overcomes the limitations of current methods, simplifies implementation, and guarantees reliable performance in the challenging environment of pipeline inspection.

This paper first reviews related work on sensor calibration (Section II) and then details our proposed calibration technique (Section III). Experimental results validating the effectiveness of our approach are presented in Section IV, followed by a discussion on the implications and potential future research directions (Section V).

II. Related Work

Calibration of laser profilers has been a significant focus of research due to its critical importance in industrial applications. Various methods have been developed to enhance the accuracy and efficiency of these sensors.

One of the notable approaches is the plane laser calibration method, as in [5]. This method uses a planar

*This work was supported by Pilgrim Technology and ANRT
[1]The author is with Pilgrim Technology, 3 rue Thomas Edison, 44118 La Chevrolière, France oho@pilgrim-technology.com
[2]The authors are with CESI LINEACT Laboratory, France. vvauchey@cesi.fr; anaitchabane@cesi.fr; ydupuis@cesi.fr

laser projection, with calibration achieved through a two-step process: initial multi-position binocular-structured light calibration and subsequent refinement using a standard ring gauge. This approach addresses systematic errors and improves measurement accuracy, but requires several calibration locations and complex optimization processes.

Other works, such as [6], have focused on manual adjustment techniques. These involve aligning the laser and camera using custom-machined calibration blocks and manual iterative adjustments. Although providing high precision, these methods are labor intensive and time consuming.

A more accurate method, as described in [7], involves using a planar chessboard to calculate the transformation between the camera and the chessboard. They then extracted the laser light in pixels and reconstructed it in 3D with respect to the laser frame, then calculated the plane of laser in the camera frame after taking a large number of images. This type of calibration is suitable for semi-planar lasers; however, it is unsuitable for planar or conic lasers with a 360-degree range.

Alternatively, the cone calibration method has been extensively explored, as described by the authors in [8]. This method involves using a conic mirror to reflect the laser beam, creating an elliptical intersection on a plane. The calibration is performed using stereo cameras to capture multiple images of the ellipse, allowing for precise determination of the cone axis equation. This technique is particularly effective for conic surfaces but requires computationally intensive optimization, and complex setups using stereo that need stereo calibration which in turn affects the results and precision.

Despite significant advancements in calibration techniques, there remains a critical need for a unified approach that leverages the strengths of existing methods while addressing their limitations. To address this gap, we introduce a novel calibration method. This method is uniquely designed to be compatible with both cone- and plane-type calibrations, providing a robust and versatile solution for industrial laser profiler calibration. Unlike previous methods that require the capture of a large number of images, our approach significantly reduces the number of images needed, simplifying the calibration process while maintaining high accuracy and efficiency.

III. METHODOLOGY

An initial laser profiler, shown in Figure 2, was developed for in-pipe inspection, using a conic mirror to enhance the laser projection and mapping process. The calibration of the laser profiler involved determining the intrinsic matrix K and distortion parameters of the camera using Zhang's method [9]. This process utilized 50 standard chessboard images captured with a GoPro in Standard Camera mode. The intrinsic matrix K is defined as:

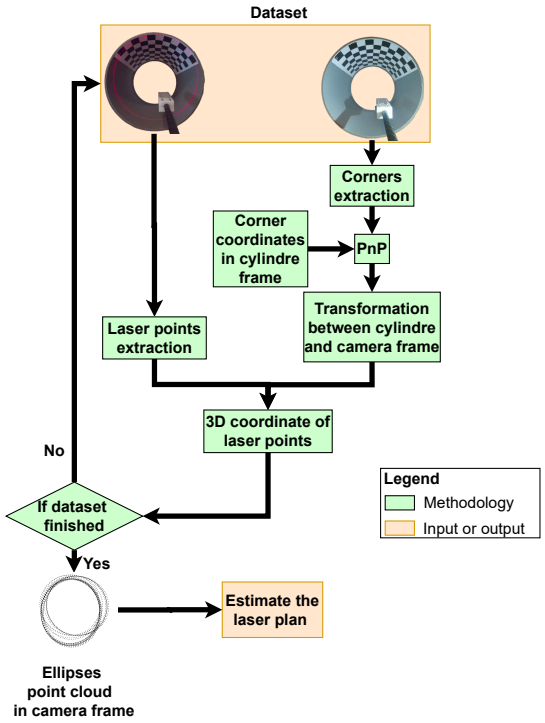

Fig. 3: Diagram Showing the Laser-Camera Calibration Method by Extracting the Point Cloud and Calculating the Laser Plane Relative to the Camera.

$$K = \begin{bmatrix} f_x & 0 & c_x \\ 0 & f_y & c_y \\ 0 & 0 & 1 \end{bmatrix} \tag{1}$$

where (f_x, f_y) are the focal lengths and (c_x, c_y) are the optical centers.

Since the intrinsic matrix K assumes an ideal pinhole camera, lens distortion must be corrected using distortion coefficients $[k_1, k_2, p_1, p_2, k_3]$. Radial distortion, addressed by k_1, k_2, and k_3, causes bulging or pinching of image points based on their distance from the center, while tangential distortion, corrected by p_1 and p_2, results from lens misalignment, leading to skewed images.

The pixel coordinates are corrected as follows:

$$x_u = x_d\left(1 + k_1 r^2 + k_2 r^4 + k_3 r^6\right) + 2p_1 x_d y_d + p_2\left(r^2 + 2x_d^2\right) \tag{2}$$

$$y_u = y_d\left(1 + k_1 r^2 + k_2 r^4 + k_3 r^6\right) + p_1\left(r^2 + 2y_d^2\right) + 2p_2 x_d y_d \tag{3}$$

where (x_u, y_u) are the corrected coordinates and (x_d, y_d) are the original distorted coordinates.

We developed a laser profiling sensor, shown in Figure 2, which consists of two main components: the laser projection part and the camera part. In the laser projection part, a conic mirror projects the laser beam onto a plane called the laser plane (L_p), the red plane in Figure 1. Positioned behind the laser at a fixed distance, the camera captures the projected laser. The calibration step allows

us to compute the equation of L_p with respect to the camera frame. As previously mentioned, the calibration between the camera and laser is crucial for enhancing the sensor's accuracy. We have introduced a new calibration method suitable for both conic and planar lasers. In this study, we elucidate the planar example, while a future study will address the conic example. In the remainder of this paragraph, we will explain the methodology outlined in Figure 3 to calibrate our sensor.

1) Dataset: We aligned the chessboard with the axis of a tube of radius r, using it as a calibration pattern, as in Figure 4. As shown in Figure 1, we fixed the laser profiler, with the camera frame $\mathcal{F}_{\text{camera}}$, behind this pattern, with his variable frame $\mathcal{F}^i_{\text{cylinder}}$ in image i, where i represents the image index, ranging from 0 to I minus one, as we captured a total of I images for laser calibration. We recorded two types of images for each position of the calibration pattern: one with the laser to extract the laser ellipse and the other without it. We varied the orientation and position of the calibration pattern and captured multiple pairs of images. For each image, we calculated the transformation between $\mathcal{F}^i_{\text{cylinder}}$ and the fixed frame $\mathcal{F}_{\text{camera}}$.

2) Cylinder frame and corner coordinates: We consider the z-axis in the cylinder frame, $\mathcal{F}^i_{\text{cylinder}}$, to be parallel to the cylinder axis, as shown in Figure 4. The x-axis, depicted in red, points towards the first corner (the yellow in the figure) of the chessboard. The y-axis, shown in green, is perpendicular to both the z-axis and x-axes. Regarding the coordinates of the corners in $\mathcal{F}_{\text{cyl}}$, Figure 4 illustrates an example of two rows of points with the same z value at each row. The yellow points have z equal to zero and the green points have z equal to square length, H, corresponding to the chosen chessboard square size. In the remainder of this article, the index j denotes the corner index. So $z^{ij}_{cylinder}$ is constant within the same row and, for row k, is given by:

$$z^{ij}_{cylinder} = 2,5.k \tag{4}$$

where k ranges from 0 to the total number of rows, $Rows$, minus one. Concerning the coordinates x and y of each row of points:

$$x^{ij}_{cylinder} = r.cos(\theta^j) \tag{5}$$

$$y^{ij}_{cylinder} = r.sin(\theta^j) \tag{6}$$

Here, the index j varying from 0 to number of corners, J, minus one. The index r represents the radius of the pipe and θ^j is the angle of the corner j in the same row, the corners in the same column have the same θ. θ^j can be calculated by dividing the linear distance of the arc between two successive corners by the radius of the pipe. $x^{ij}_{cylinder}$ and $y^{ij}_{cylinder}$ are the coordinates of a corner j in image i with respect to the cylinder frame, $\mathcal{F}^i_{\text{cylinder}}$.

3) Corner extraction in images and PnP: The diagram in Figure 3 illustrates the calibration steps pipeline. After capturing the datasets, we extract the corners of the chessboard in the pixel frame.

The relations between camera, pixel and cylinder coordinates are:

$$\begin{bmatrix} x^{ij}_{\text{camera}} \\ y^{ij}_{\text{camera}} \\ z^{ij}_{\text{camera}} \end{bmatrix} = s^{ij} \cdot \left(K^{-1} \cdot \begin{bmatrix} u^{ij} \\ v^{ij} \\ 1 \end{bmatrix} \right) \tag{7}$$

$$s^{ij} \begin{bmatrix} u^{ij} \\ v^{ij} \\ 1 \end{bmatrix} = [K] \begin{bmatrix} R^i & t^i \end{bmatrix} \begin{bmatrix} x^{ij}_{cylinder} \\ y^{ij}_{cylinder} \\ z^{ij}_{cylinder} \\ 1 \end{bmatrix} \tag{8}$$

Where s^{ij} represents the depth information for corner j in image i, which is z_{cam}, (u^{ij}, v^{ij}) are the pixel coordinates. $x_{cylinder}$, $y_{cylinder}$ and $z_{cylinder}$ are the coordinates of the corner in $\mathcal{F}_{\text{cylinder}}$, and x_{camera}, y_{camera} and z_{camera} are the coordinates of a point in $\mathcal{F}_{\text{camera}}$. R^i and t^i denote the rotation and translation in image i, respectively, between the cylinder and camera coordinates.

Using the (u, v) pixel for all corners in image i, and their coordinates in $\mathcal{F}^i_{\text{cylinder}}$, the translation and rotation in each image between $\mathcal{F}^i_{\text{cylinder}}$ and $\mathcal{F}_{\text{camera}}$ are estimated using the perspective n-point, PnP, algorithm [10].

4) Laser plane equation: To calculate the laser plane in the image i, we extracted and then fitted the laser ellipse, as in Figure 4, using pixel intensity and OpenCV, particularly the fitEllipse function in OpenCV [11]. This laser represents the intersection between the cylinder surface in 3D and the laser ray extracted from the pixel. To determine the coordinates in $\mathcal{F}^i_{\text{cylinder}}$ and $\mathcal{F}_{\text{camera}}$, we began by establishing the relationship between the coordinates between these two frames:

The index l denotes the laser point. For each red laser pixel, after substituting the constants in the matrices and replacing the l-th laser pixel point (u^{il}, v^{il}), in image i, with those of the laser pixels, we can rewrite equation **??** in an alternative form:

$$\begin{bmatrix} x^{il}_{\text{cylinder}} \\ y^{il}_{\text{cylinder}} \\ z^{il}_{\text{cylinder}} \end{bmatrix} = s^{il} \cdot \begin{bmatrix} a^{il} \\ b^{il} \\ c^{il} \end{bmatrix} + \begin{bmatrix} t^i_{2x} \\ t^i_{2y} \\ t^i_{2z} \end{bmatrix} \tag{9}$$

The coordinates of the points in $\mathcal{F}_{\text{cyl}}$, for a cylinder with radius r, should satisfy the following cylinder equation:

$$x^{il}_{\text{cylinder}}{}^2 + y^{il}_{\text{cylinder}}{}^2 = r^2 \tag{10}$$

The laser points represent the intersection between the camera ray and the surface of the cylinder. To calculate the unknown s^{il}, we use the equation 9 in conjunction with the cylinder equation 10. This yields a second equation with one unknown:

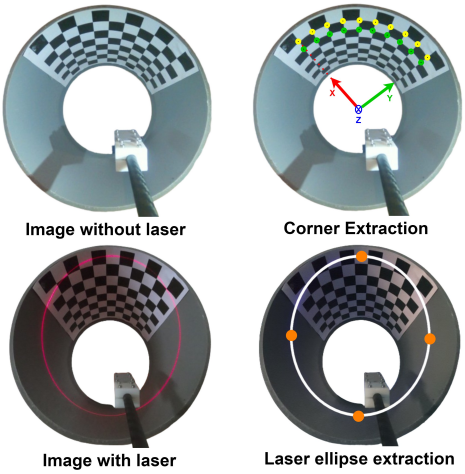

Fig. 4: Top - First two rows of corners extracted with cylinder frame; Bottom - Laser ellipse extraction with four endpoints.

$$\left(s^{il}\cdot a^{il}+t^{i}_{2x}\right)^2+\left(s^{il}\cdot b^{il}+t^{i}_{2y}\right)^2=r^2 \qquad (11)$$

Solving the quadratic equation 11 yields two solutions: one positive and one negative. Since s^{il} represents the depth Z^{il}_{camera} of the point laser l, it must be positive. Therefore, the valid solution is the positive one. Using equations 9 and 7, we calculated the coordinates x^{il}_{camera}, y^{il}_{camera} and z^{il}_{camera} for each point l on the laser ellipse. We then stored all these ellipse points of this image in a matrix called $plan-laser-points$ as in Figure 3. All these coordinates, in the camera frame, lie on the laser plane.

Performing this step for all laser pixels allows us to reconstruct the ellipse from 2D to 3D.

Repeating this step for each of the 21 images generates a point cloud containing the reconstructed ellipses in 3D with respect to $\mathcal{F}_{\text{camera}}$. All these ellipses points stored in $plan-laser-points$, lie in the same laser plane and form the point cloud shown in Figure 3, and we used these points to estimate the laser plane equation with respect to $\mathcal{F}_{\text{camera}}$. The resulting plane equation of the laser was determined to be:

$$\alpha\cdot x+\beta\cdot y+\gamma\cdot z+1.00=0 \qquad (12)$$

In the case of cone-laser systems, the equations governing cone geometry, as described in [8], remain applicable. However, the primary advantage of our method is its ability to exploit the point cloud of ellipses on the cone surface to precisely determine the cone axis. This process begins with calculating the axis using the centers of the ellipses. The angle of the cone is then determined. Finally, the cone's center, defined as a point along its axis relative to the camera frame, is computed. The methodology for utilizing the points on the ellipses to perform these calculations is both straightforward and computationally efficient.

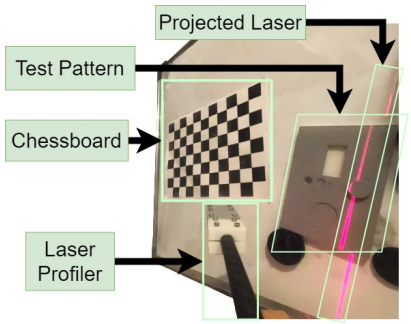

Fig. 5: Evaluation of the 3D Reconstruction Process Using a Chessboard Pattern for Camera Pose Estimation

Parameter	Value		Parameter	Value
f_x	1.9356×10^3		p_1	-0.00468
f_y	1.9317×10^3		p_2	-0.00218
c_x	1.9900×10^3		k_3	0.0924
c_y	1.4751×10^3		r (cm)	12.5
k_1	0.04596		*Rows*	11
k_2	-0.0791		*Columns*	8
J	69		α	-0.0005
β	0.0024		γ	-0.0449
I	21		H (cm)	2.5

TABLE I: Parameters and Corresponding Values Used in the Experiment

IV. EXPERIMENTS AND RESULTS

Table I presents the values of the parameters used in our experimental process.

To evaluate the performance of our proposed calibration method, we conducted experiments using a hand-held approach. Specifically, our goal was to quantify the error in the diameter measurements of the calibrated pipes, as well as the error in the 3D reconstruction.

The inner surface of a standard cylinder is ideally a perfect cylindrical surface. When a light plane intersects this inner surface, it generates an ellipse, where the length of the minor axis corresponds to the inner diameter of the cylinder [12], [5].

The minor axis lengths were compared with the known inner diameter of the cylinder, allowing us to calculate the errors in our measurements. Through this process, we confirmed that the errors in the diameter measurements and 3D reconstruction were minimal, demonstrating the efficacy and accuracy of our proposed calibration technique.

A. Hardware Overview

For the initial version of our laser profiler sensor in figure 2, we employed a GoPro Hero 8 Black camera and a red laser module (Module laser red 650nm 1mW [13]). The laser intensity was controlled using an Arduino UNO. The GoPro captured and stored images on a SD card, while the Arduino provided the necessary 5V power supply for the laser. Offline processing of the captured data was performed on an Asus laptop equipped with an Intel(R) Core(TM) i5-9300H CPU @ 2.4 GHz.

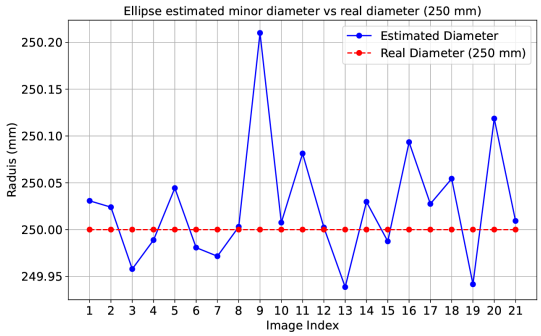

Fig. 6: This plot illustrates the difference between the estimated diameter and the actual diameter.

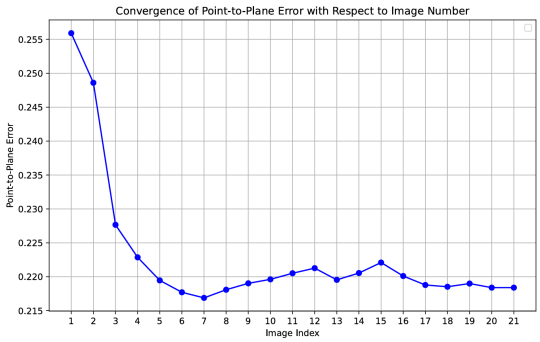

Fig. 7: Least Square Error between the point cloud of ellipses and the 21 approximated planes.

B. Minor Diameter

Figure 6 shows the minor diameter error for 21 images, where the red plot shows the actual diameter of the pipe, and the blue plot shows the estimated diameter in each of the 21 images. In our study, we used a pipe with a diameter of 250 mm. The maximum observed diameter was in image nine, measuring 250.22 mm, resulting in a maximum error of 0.22 mm.

To determine the suitable number of datasets needed to ensure high precision for the calibration and reconstruction of our proposed sensor, we calculated the estimated plane after each new image. In image n, we used the estimated 3D ellipses from images 1 to n to calculate the estimated plane for image n. We obtained 21 estimated planes in total. We then calculated the re-projection error between the point cloud of all estimated ellipse points and the estimated planes after each new image.

Figure 7 shows the convergence of the re-projection error after 5 images. This is a significant advantage of our method. With only five images, we can calibrate our sensor with high precision.

C. Reconstruction

To test our calibration, one needs to scan a test pattern (Figure 8) in 3D, with knowledge of dimensions. We utilized Inventor CAD 2024 to design a rectangular test pattern featuring a circular aperture, which was

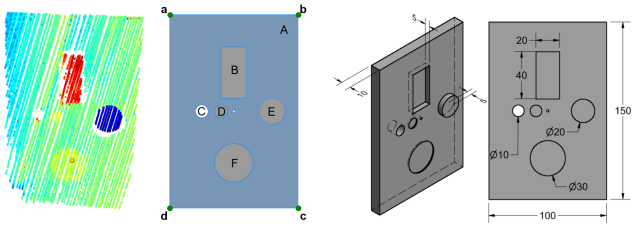

Fig. 8: Point Cloud Output of the Test Pattern (left), with Labeled Planes (middle) and testing pattern dimensions in millimeters (right).

subsequently fabricated using a CNC machine with a precision tolerance of 0.5 mm. The dimensions were verified post-fabrication using a caliper to ensure measurement accuracy. We chose a circular shape because it is possible to achieve the real diameter during the scan and calculate the error.

To scan it, we used a chessboard as the world frame $\mathcal{F}_{\text{world}}$, as in Figure 5, to determine the pose of the camera with respect to it.

After knowing the plane of laser in $\mathcal{F}_{\text{cam}}$ in the calibration step, the laser point cloud in 3D in each image is the intersection between the pixel ray and and the laser plane. To reconstruct the plaque with respect to a fixed frame ($\mathcal{F}_{\text{chess}}$) We used the transformation between $\mathcal{F}_{\text{cam}}$ and $\mathcal{F}_{\text{chess}}$ to transform the laser points from $\mathcal{F}_{\text{cam}}$ to $\mathcal{F}_{\text{chess}}$. The preceding verification method indicated that with a diameter of 25 cm, the maximum error in our calibration was 0.22cm, observed in image number nine. To further validate our calibration method, we should test our sensor on pipes with different radii or reconstruct a test pattern, similar to the approach in [2][3], which involves varying pipe sizes, as shown in Figure 5. We opted for the latter approach and captured 110 images from different positions after fixing the test pattern relative to the chessboard. We changed the position of the sensor after each image to cover the entire surface of the test plaque, as illustrated in Figure 5.

Figure 8 shows us the name for each plane in the test pattern, 'A' is the background, 'C, D, E and F' are the four circular holes in the plaque, and 'B' is the rectangular one.

We applied the least squares method to estimate the plane of surface 'A', and subsequently computed the maximum, minimum, and average errors between the actual and estimated distances from the point clouds of surfaces 'B, E, and F' to the estimated plane of 'A'.

Table II summarizes the real absolute distance between plane A and points on planes B, E, and F, along with error characteristics during the reconstruction step (maximum error, mean error and standard deviation (stdev)). Key findings include real distances of 5 mm for pairs (B, A) and (E, A), and 1 mm for (F, A). The highest maximum error is 0.8864 mm for (B, A), with mean errors lowest for (B, A) at 0.2224 mm and

highest for (F, A) at 0.3135 mm. The standard deviation is highest for (F, A) at 0.2023 mm. These confirms that the absolute point-to-plane error is less than 0.9 mm. These findings indicate the effectiveness of the methods and their potential for precise distance estimation.

	Real Dist	Error Characteristics		
		Max	Mean	Stdev
B, A	5	0.8864	0.2224	0.1942
E, A	5	0.8287	0.2404	0.1589
F, A	1	0.8641	0.3135	0.2023

TABLE II: Real and estimated depths between surfaces in millimeters (mm).

Length	Real Dist.	Est. Dist.	Abs. Error
ab	10	10.0368	0.0368
bc	15	14.9854	0.0146
C diameter	1	1.0883	0.0883
D diameter	1	1.0195	0.0195
E diameter	2	1.9243	0.0757
F diameter	3	2.9181	0.0819

TABLE III: Difference between real and estimated distance (diameter or lengths) on the test pattern (measured in cm), along with the corresponding absolute error.

Analyzing the true diameter of circles C, D, E, and F on the test pattern of Figure 8, in conjunction with the estimated radii, and the actual lengths ab and bc, as illustrated in Table III, reveals that the maximum absolute error is 0.0883 cm. This confirms that the absolute point-to-point error remains well below 0.1 cm, demonstrating sufficient accuracy for the inspection and reconstruction of pipes in future work. These results demonstrate the precision of the measurement methods, with errors consistently remaining below 1 mm, thus validating the reliability of the reconstruction process.

In comparison with a study from the literature validating the reliability of the reconstruction process, the visual-inertial-LiDAR-laser SLAM approach described in [3] achieves a per-point local scanning error of less than 0.88 mm within a 12-inch diameter pipe over a mapping distance of 22 meters. In our implementation, the observed per-point local scanning error was 0.8864 mm, slightly higher due to accuracy limitations in camera localization. This performance could be further improved by integrating advanced multi-sensor SLAM techniques.

V. Summary and future research directions

This study presented a novel laser profiler sensor and a customized calibration method specifically designed for accurate pipe inspection. The key contributions of this work include a data-efficient and highly accurate calibration approach utilizing a curved chessboard to determine the cameras spatial position, as well as an ellipse-fitting method combined with corner coordinate computation via the PnP algorithm. Validation results demonstrated that the calibration error consistently remained below 1 mm. Future research will aim at integrating the sensor into in-pipe robotic systems, enhancing SLAM and odometry transformation algorithms, and conducting field tests to further validate the sensors effectiveness in real-world pipe inspection scenarios.

ACKNOWLEDGMENT

The authors thank Pilgrim Technology for providing the testing facilities. The authors also acknowledge the financial support of ANRT (National Association of Research and Technology) for funding this research work nř2023/0735.

References

[1] V. B. Sharma, S. Tewari, S. Biswas, and A. Sharma, "A comprehensive study of techniques utilized for structural health monitoring of oil and gas pipelines," *Structural Health Monitoring*, vol. 23, no. 3, pp. 1816–1841, 2024.

[2] D. Cheng, H. Shi, A. Xu, M. Schwerin, M. Crivella, L. Li, and H. Choset, "Visual-laser-inertial slam using a compact 3d scanner for confined space," in *2021 IEEE International Conference on Robotics and Automation (ICRA)*, pp. 5699–5705, IEEE, 2021.

[3] T. Tian, L. Wang, X. Yan, F. Ruan, G. J. Aadityaa, H. Choset, and L. Li, "Visual-inertial-laser-lidar (vill) slam: Real-time dense rgb-d mapping for pipe environments," in *2023 IEEE/RSJ International Conference on Intelligent Robots and Systems (IROS)*, pp. 1525–1531, IEEE, 2023.

[4] J. Fan, Y. Ou, X. Li, C. Zhou, and Z. Hou, "Structured light vision based pipeline tracking and 3d reconstruction method for underwater vehicle," *IEEE Transactions on Intelligent Vehicles*, 2023.

[5] Y. Dong, C. Fang, L. Zhu, N. Yan, and X. Zhang, "The calibration method of the circle-structured light measurement system for inner surfaces considering systematic errors," *Measurement Science and Technology*, vol. 32, no. 7, p. 075012, 2021.

[6] W. Jackson, G. Dobie, C. MacLeod, G. West, C. Mineo, and L. McDonald, "Error analysis and calibration for a novel pipe profiling tool," *IEEE Sensors Journal*, vol. 20, no. 7, pp. 3545–3555, 2019.

[7] D. Cheng, H. Shi, M. Schwerin, M. Crivella, L. Li, and H. Choset, "A compact and infrastructure-free confined space sensor for 3d scanning and slam," in *2020 IEEE SENSORS*, pp. 1–4, IEEE, 2020.

[8] Y. Zhu, Y. Gu, Y. Jin, and C. Zhai, "Flexible calibration method for an inner surface detector based on circle structured light," *Applied Optics*, vol. 55, no. 5, pp. 1034–1039, 2016.

[9] Z. Zhang, "A flexible new technique for camera calibration," *IEEE Transactions on pattern analysis and machine intelligence*, vol. 22, no. 11, pp. 1330–1334, 2000.

[10] V. Lepetit, F. Moreno-Noguer, and P. Fua, "Ep n p: An accurate o (n) solution to the p n p problem," *International journal of computer vision*, vol. 81, pp. 155–166, 2009.

[11] OpenCV, "Shape descriptors." `https://docs.opencv.org/4.x/d3/dc0/group__imgproc__shape.html`, 2024. Accessed: 2024-07-24.

[12] L. Jin, N. Miyatsu, E. Kondoh, B. Gelloz, N. Kanazawa, and T. Yoshizawa, "Measurement of diameter of cylindrical openings using a disk beam probe," *Optical Review*, vol. 25, pp. 656–662, 2018.

[13] "Laser module." `https://fr.rs-online.com/web/p/modules-laser/0105013`. Accessed: 2024-07-19.